Journal of
Materials Chemistry C

PAPER

View Article Online
View Journal | View Issue

Cite this: *J. Mater. Chem. C*, 2018, **6**, 9181

Understanding quantum confinement and ligand removal in solution-based ZnO thin films from highly stable nanocrystal ink†

Yuhang Sun,[a] Preston D. Donaldson,[a] Javier Garcia-Barriocanal[b] and Sarah L. Swisher*[a]

Received 2nd April 2018,
Accepted 3rd August 2018

DOI: 10.1039/c8tc01536h

rsc.li/materials-c

We report a synthesis procedure for dodecanethiol capped wurtzite ZnO nanocrystals with an average diameter of 4 nm that are monodisperse, highly soluble, and shelf-stable for many months. Compared to previous ZnO ink recipes, we demonstrate improved particle solubility and excellent ink stability, resulting in ZnO nanocrystal inks that are optimized for printed electronics applications. The ZnO nanocrystal solution exhibits an absorption peak at 341 nm (3.63 eV), which represents a blue-shift of approximately 0.3 eV from the bulk ZnO bandgap (∼3.3 eV). This blue shift is consistent with previously reported models for an increased bandgap due to quantum confinement. We used variable-angle spectroscopic ellipsometry (VASE) to determine the optical properties of solution-processed thin films of ZnO nanocrystals, which provides valuable insight into the changes in film composition and morphology that occur during thermal annealing treatments ranging from 150–300 °C. The ZnO nanocrystals maintain their quantum confinement when deposited into a thin film, and the degree of quantum confinement is gradually reduced as the thermal annealing temperature increases. Using infrared absorption measurements (FTIR) and X-ray photoelectron spectroscopy (XPS), we show that the dodecanethiol ligands are removed from the ZnO films during annealing, resulting in a high-purity semiconductor film with very low carbon contamination. Furthermore, we show that annealing at 300 °C results in complete ligand removal with only a slight increase in grain size. Thin-film transistors (TFT) using ZnO nanocrystals as the channel material annealed at 300 °C show moderate mobility ($\sim$0.002 $cm^2\ V^{-1}\ s^{-1}$) and good on/off ratio $>10^4$. These results demonstrate the distinct advantages of colloidal nanocrystals for printed electronics applications: the composition and morphology of the solution-processed film can be carefully tuned by controlling the size and surface coating of the nanocrystals in the ink.

Introduction

Solution-processed electronic materials have been the focus of intense research efforts in recent years, especially as an attractive route towards large-area flexible electronics. Mechanical flexibility results in lightweight and robust electronic devices that are less likely to shatter or fracture, and also allows electronics to be more easily integrated with the body for health and fitness monitoring, medical devices, and wearable electronics.

Despite these recent efforts, the performance of solution-processed semiconductor materials still lags behind standard gas-phase deposition processes, particularly when thermal processing steps are limited to plastic-compatible temperatures. High-quality solution-processed semiconductors on low-cost plastic substrates are needed to meet the demands of next-generation flexible electronics applications. To meet this challenge, there has been a surge[1–6] of effort to develop solution-processed electronic materials and devices that do not require high-temperature processing or etching, both of which limit the use of flexible substrates.

The two most widely used synthesis strategies for solution-based electronics are sol–gels and colloidal nanocrystals.[7] Sol–gels provide an easy and versatile approach in which precursors are mixed in solution, deposited onto a substrate, and then heated to convert the precursors into the desired material. Two significant limitations arise as a result of this conversion happening on the substrate. First, the thermal budget of the substrate often results in suboptimal film conversion. Second, sol–gel inks are sensitive to precursor preparation and aging time. The ink can degrade if the timing is not precisely controlled during device processing, which leads to inconsistent device performance.

Colloidal nanocrystals provide an alternative route to printable semiconductor inks. In contrast to sol–gels, colloidal nanocrystals are synthesized and encapsulated with organic ligand molecules prior to deposition onto the substrate. Nanocrystal thin films typically require some post-deposition processing to remove

---

[a] *Department of Electrical and Computer Engineering, University of Minnesota, 200 Union Street SE, Minneapolis, Minnesota, 55455, USA. E-mail: sswisher@umn.edu*
[b] *Characterization Facility, University of Minnesota, Minneapolis, MN 55455, USA*

† Electronic supplementary information (ESI) available. See DOI: 10.1039/c8tc01536h

organic residue and improve electronic transport through the film, but – unlike sol–gel films – there are no precursors that must be converted to the desired material. This is a significant advantage of nanocrystals over sol–gels for flexible electronics: the thermal energy required to form the desired material is decoupled from the thermal budget of the substrate. Nanocrystals also provide unique size-tunable physical properties and can easily be dispersed in organic solvents, making them attractive candidates for active layers in advanced optoelectronic devices and thin film electronics.[8,9] The development of synthesis strategies for solution based nanocrystals, such as precisely controlling the growth of nanocrystals,[10] will help pave the way toward printable electronic devices.

Much of the work on colloidal semiconductor nanocrystals has focused on chalcogenides (CdSe, CdTe, *etc.*). However, semiconductor inks based on ZnO nanocrystals are more air-stable and less toxic, which are key advantages for large-area printed electronics. Bulk and thin-film ZnO have been used for decades in a variety of applications including UV-detectors,[11–13] solar cells,[14,15] gas sensors,[16] electronic memories,[17,18] and thin film waveguides.[19] ZnO thin films are also widely studied (often in combination with In, Ga, or Sn) for the active channel layer in thin-film transistors.[3,20–23]

Previously, thin films of ZnO have typically been deposited using conventional vacuum-based deposition processes such as rf magnetron sputtering, chemical vapor deposition (CVD), and pulsed-laser deposition (PLD).[24] However, next generation thin-film devices demand processing techniques that can produce robust, lightweight, large-area devices on low-cost flexible substrates. Printing is well-suited to this task,[25] so printable ZnO inks are needed. As previously discussed, ZnO inks made from colloidal nanocrystals will provide substantial benefits over sol–gel formulations. Nanocrystals of ZnO with various of diameters have been obtained by a variety of liquid phase processes.[10,26–29] Investigations into the optical properties of ZnO nanocrystals are of great interest, and exploration of the optical properties has demonstrated that the bandgap in ZnO nanocrystals is strongly size-dependent below a diameter of 7.0 nm.[30] For example, in one of the early reports, Mahamuni *et al.*[31] synthesized well-crystallized ZnO nanoparticles with an average diameter of 6.1 nm, and observed an excitonic absorption peak that was significantly blue-shifted from the bulk ZnO bandgap of ~3.3 eV.[24] Several other groups have since reported synthesis routines for ZnO nanocrystals in the 2–15 nm size range.[26,32–34] Some of these procedures result in particles that tend to aggregate in solution (possibly indicating insufficient surface encapsulation), but many have observed quantum confinement effects nonetheless.

Although the synthesis procedures for colloidal ZnO nanocrystals and the optical properties of those colloidal solutions have been studied for many years, one of the most promising uses for nanocrystal dispersions is solution-processed thin films for printed flexible electronics. For this application, small nanocrystals are generally preferred because they may provide (1) smaller minimum printed feature sizes[35] and (2) a lower melting point.[36] It is important to consider what is known about colloidal ZnO nanocrystals from the point of view of printed electronics. For example, though ultra-small nanocrystals exhibit significant quantum confinement in the solution phase, it is expected that the optical properties will be significantly altered when the nanocrystal solution is printed, dried, and converted to a thin film. Ultimately, it is the final properties of the thin film that are of vital importance for printed electronics applications. Quantum confinement will dramatically change fundamental aspects of the film, including the bandgap, free carrier concentration, and carrier transport mechanisms. Thus, if a colloidal ZnO nanocrystal ink is used to fabricate a ZnO thin-film transistor, the transistor performance will be strongly impacted by the degree of quantum confinement of the ZnO nanocrystals in the thin film. This illustrates why a better understanding of the relationship between the semiconductor ink, the thin film fabrication process, and the performance of devices and circuits is needed before semiconductor nanocrystal inks can be fully leveraged for printed electronics applications.

In this work, we have synthesized well-encapsulated, ultra-small ZnO colloidal nanocrystals with a narrow size distribution around 4 nm in diameter. In the liquid phase, these ZnO nanocrystal inks exhibit significant quantum confinement and thus an increased bandgap. We have employed standard processing techniques used during the fabrication of flexible electronics, then studied how the conversion from colloidal ink to a thin film impacts the optical properties, chemical composition, and crystallite size. Variable-angle spectroscopic ellipsometry (VASE) is a widely-used technique for probing the optical constants of thin films, but VASE thin film analysis has not been reported in previous studies of ultra-small colloidal ZnO nanocrystals. Combining VASE analysis with infrared absorption (FTIR), X-ray photoelectron spectroscopy (XPS) and grazing incidence X-ray diffraction (GIXRD) measurements, we have studied changes in the optical properties, the chemical composition, and the morphology of ZnO nanocrystal films after thermal annealing. We show that ZnO nanocrystal thin films exhibit significant quantum confinement. Subsequent thermal annealing of the ZnO nanocrystal films at moderate temperatures (200–300 °C) recovers the bulk ZnO bandgap and efficiently removes organic ligand residue, but very little grain growth is observed. Films of ZnO nanocrystals annealed at 300 °C are used to form the channel layer of a thin-film transistor (TFT), demonstrating that removing the ligands enables the onset of transistor behaviour. This is vital information for the design of ZnO thin film devices. Furthermore, we show that nanocrystal inks are extremely stable in solution, with no changes observed over at least 7 months. Insight from this work will provide a better understanding of how to design printable semiconductor inks that will result in high-quality solution-processed thin films for printed electronics applications.

Experimental methods

Materials

Zinc acetate dihydrate (CAS: 5970-45-6, ≥98%), sodium hydroxide (CAS: 1310-73-2, >97%), and 1-dodecanethiol (CAS: 112-55-0, >98%) were purchased from Aldrich and used as received.

ZnO nanocrystal synthesis

ZnO nanocrystals were prepared by a procedure similar to that reported previously by Volkman *et al.*[37] A solution of zinc acetate dihydrate (1 g = 45 mmol) in isopropanol (250 mL) was heated to 60 °C in oil bath. Meanwhile, NaOH (0.29 g = 73 mmol) was dissolved in 85 mL of isopropanol at room temperature. The NaOH solution was added to the flask containing the zinc solution, and the reaction temperature was maintained at 60 °C. After 30 minutes, the encapsulant 1-dodecanethiol (1. 09 mL) was added dropwise. Turbidity started to appear after adding in 1-dodecanethiol. Both heating and stirring ceased after 60 minutes and the dispersion was left to sediment. The supernatant was removed, and the nanocrystal content was transferred into 50 mL centrifugation tubes. Ethanol was added to the tubes to clean the particles, and the ZnO nanocrystals were precipitated by centrifugation at 3500 rpm for 2 minutes. The ethanol cleaning process was repeated two more times. Finally, the ZnO nanocrystals are collected and redispersed in 10 mL of chloroform.

ZnO nanocrystal thin film preparation

Films of ZnO nanocrystals were deposited onto silicon substrates for ellipsometry, FTIR, and XPS measurements. The silicon substrates were cleaned using 3-step sonication (toluene, acetone and isopropanol) for 15 minutes each, then dried under a flow of nitrogen. The ZnO nanocrystal films were spin-coated (Laurel WS-650-8B) using as-prepared ZnO dispersions without any other post-synthesis processing. Thin, uniform films were obtained by dropping approximately 0.1 mL of ZnO nanocrystal dispersion onto the stationary substrate, then using a two-step spin program (1000 rpm for 10 s, then 3000 rpm for 20 s). The films were stored in air at room temperature. The thickness of the deposited nanocrystal film was found to be approximately 40 nm thick according to the VASE analysis and confirmed with profilometry. The ZnO thin films were annealed in a tube furnace for 90 minutes at 210 °C or 300 °C. The thickness of annealed films was found to be approximately 20 nm and 15 nm, respectively, according to VASE analysis. For GIXRD analysis, a thicker ZnO film was required to obtain sufficient signal counts. Therefore, a two-layer ZnO nanocrystal film was prepared with a second layer spun on top after drying the first layer at 60 °C on a hotplate for 1 hour. The film was then annealed in the tube furnace at 300 °C for 90 minutes.

Material characterization

UV-visible absorption spectra of the diluted ZnO nanocrystal dispersions were obtained using a Cary 5000 spectrophotometer. Transmission electron microscope (TEM) images and selected area electron diffraction (SAED) patterns were obtained using a FEI Tecnai T12 microscope with an accelerating voltage of 120 kV. For TEM imaging, one droplet of the ZnO nanocrystal dispersion was deposited onto an ultrathin carbon TEM grid (Ted Pella, #01824) and allowed to dry at room temperature. Thin-film spectroscopic ellipsometry was measured using a Variable Angle Spectroscopic Ellipsometer (J.A. Woollam Co. Inc) at incidence angles of 65°, 70°, and 75° over a wavelength range from 230 nm to 1200 nm. The data were analyzed with WVASE 32 software. Chemical composition was examined using X-ray photoemission spectroscopy, with Ar ion etching steps for depth profiling on a Surface Science SSX-100. Infrared absorption measurements were performed on a Nicolet Series Magna-IR System 750 FTIR. Grazing incidence X-ray diffraction (GIXRD) was measured using a Bruker X-ray microdiffractometer equipped with a 2-dimensional detector (Vantec 500) and a Co X-ray source (λ = 0.179 nm). The incident X-ray beam was conditioned with a graphite monochromator to eliminate the K_β contribution. Two sets of measurements were collected for incident angles 3.5° and 5° respectively. For each incident angle, two frames were collected covering a total 2θ range of 40°. XRD profiles were fitted using MDI-Jade and the instrument resolution was deconvoluted from the data using a LaB_6 reference measured under the same conditions as the ZnO sample.

Thin-film transistor fabrication and characterization

Thin-film transistor (TFT) test structures were fabricated on heavily-doped silicon wafers with 50 nm of thermally-grown SiO_2 as the gate and gate dielectric, respectively. Two-layer films of ZnO were spin-coated onto the wafer. The first layer was baked for 1 hour at 60 °C on a hotplate, the second layer was spin-coated, and then the device was annealed in the tube furnace at 300 °C for 1 hour. Source/drain electrode patterns were lithographically defined, and Aluminum was sputtered (AJA Sputterer) with argon. Aluminum was lifted off by sonicating in Microposit Remover 1165 for 20 minutes. TFT transfer and output curves were measured using a Keysight B1500 semiconductor parameter analyser. All devices were measured in shielded enclosure in ambient air.

Results and discussion

Synthesis and characterization of 4 nm ZnO nanocrystals

In printed electronics, metal nanoparticle inks are commonly used for conductive portions of a circuit.[38,39] Smaller nanoparticles are desirable because printed feature sizes and line roughness can be minimized. Furthermore, smaller particles sinter with less heat (because of their increased surface energy), thus enabling lower processing temperatures.[40]

To extend these benefits to printed semiconductors, in this work we synthesized ultra-small ZnO nanocrystals to produce solution-processed semiconductor thin films. A bright field TEM image of the colloidal ZnO nanocrystals is shown in Fig. 1(a). The ZnO nanocrystals are roughly spherical and well-dispersed, with very little agglomeration observed. Measurements of >120 individual particles yielded an average diameter of 4.0 ± 0.79 nm. Clear rings are visible in the electron diffraction pattern (Fig. 1c) that agree well with the standard wurtzite ZnO diffraction pattern (Table 1). The ZnO nanocrystals can be easily dispersed in nonpolar solvents to form a clear, transparent ink. The excellent solubility and monodispersity presumably results from the capping molecules on the nanocrystal surface, which provide

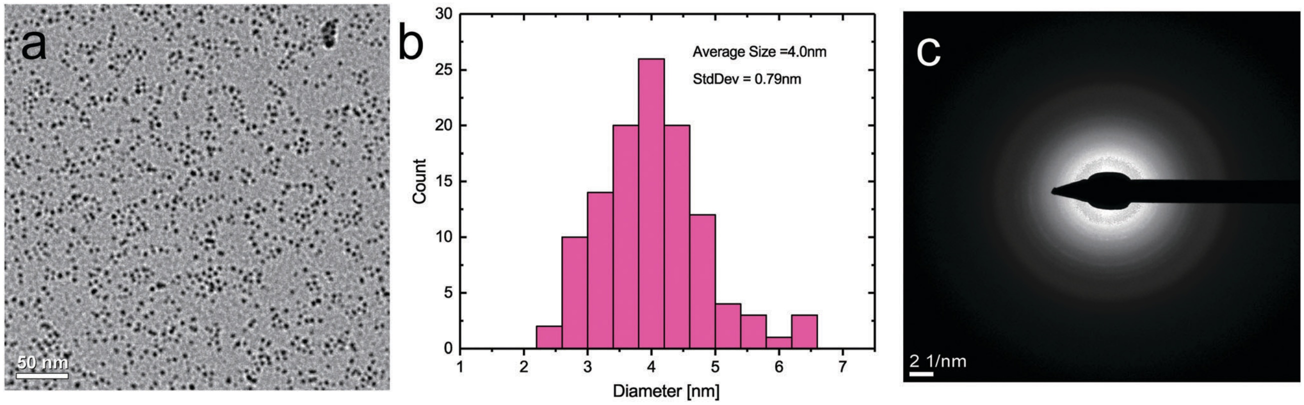

Fig. 1 (a) Transmission electron micrograph TEM of dodecanethiol-capped ZnO nanocrystals. Scale bar = 50 nm. (b) Histogram of nanocrystal diameter calculated from >120 individual particles. (c) Selected area electron diffraction (SAED) pattern of ZnO nanocrystal.

Table 1 Summary of *d*-spacing measurements from the selected area electron diffraction (SAED) patterns of the ZnO colloidal nanocrystals compared to bulk wurtzite reference values

Ring no.	$d_{\text{wurtzite}}(hkl)$ (Å)	$d_{\text{Zno NC}}(hkl)$ (Å)	*hkl*
1	2.603	2.601	(002)
2	2.476	2.452	(101)
3	1.911	1.902	(102)
4	1.625	1.621	(110)
5	1.478	1.490	(103)
6	1.378	1.374	(112)

steric forces to keep the nanocrystals from merging. Here the 1-dodecanethiol works as the encapsulant and forms a monolayer on the surface of the ZnO nanocrystals.

Fig. 2 shows the absorption spectra of our as-prepared ZnO nanocrystals in chloroform. The ZnO nanocrystals exhibit an absorption peak at approximately 341 nm (3.63 eV), which is blue-shifted from the bulk ZnO peak at 370 nm (3.35 eV). Previous studies have demonstrated that ZnO nanocrystals smaller than 7 nm diameter show a size-dependent bandgap due to quantum confinement,[41] which is consistent with our results.

In addition to extracting the bandgap, the UV-visible absorption spectrum can also provide an estimate of the nanocrystal size using a model proposed by Meulenkamp[42] in a study of the evolution of ZnO particles during aging. In that work, the size and absorption spectra of non-agglomerated ZnO sol samples were recorded. The model correlates the particle size ($2.5 < d < 6.5$ nm) with the wavelength at which the absorbance is 50% of the peak value ($\lambda_{1/2}$). As seen in Fig. 2, $\lambda_{1/2}$ for our ZnO colloidal nanocrystals is 353 nm. According to the model (see ESI†), this corresponds to a particle diameter of 3.93 nm, which is in excellent agreement with the diameter measured from the TEM images.

In order to quantify the relationship between optical absorption and nanocrystal size and explore the quantum confinement effects, the absorption energies of ZnO nanocrystals prepared by various solution-based methods are summarized in Fig. 3. Previous work[43,44] suggests that the blue-shift of the ZnO bandgap due to

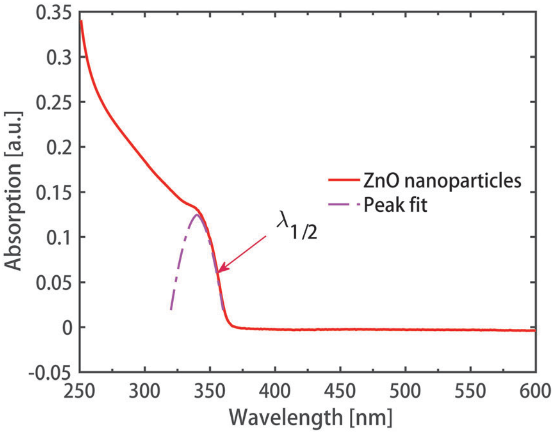

Fig. 2 UV-vis absorption spectra for the ZnO nanocrystal solution. The absorption peak is extracted from the peak fit. The wavelength at which the absorbance is 50% of the peak value, $\lambda_{1/2}$, is also indicated for reference.

the quantum confinement effect can be predicted as a function of nanocrystal radius as[45,46]

$$E_{\mathrm{G(dot)}} = E_{\mathrm{G(bulk)}} + \frac{(\pi\hbar)^2}{2R^2}\left(\frac{1}{m_e{}^*} + \frac{1}{m_h{}^*}\right) - 0.248E_{\mathrm{Ryd}}{}^* \qquad (1)$$

where is the reduced Planck's constant, R is the radius of ZnO nanocrystal, $m_e{}^*$ and $m_h{}^*$ are the effective masses of electron and hole (using $m_e{}^* = 0.24m_0$ and $m_h{}^* = 1.8m_0$),[47] $E_{\text{(gap,bulk)}}$ is the bulk ZnO bandgap (3.37 eV), and $E_{\text{Ryd}}{}^*$ is the exciton binding energy (60 meV).[48] This model is shown in Fig. 3 and compared to several experimental reports of ZnO nanocrystals.[26,27,32,49] Overall, these data exhibit a trend which is in good agreement with the model, but most of the measured bandgaps are smaller than what the model predicts. This difference is attributed to the assumption of the infinite potential barrier in the theoretical calculation,[46] while the finite potential barrier on the ZnO nanocrystals results in a slightly smaller confinement effect. Using eqn (1), we calculate the predicted bandgap of our 4.0 nm ZnO nanocrystals to be 3.72 eV. This is in very good agreement with the absorption peak

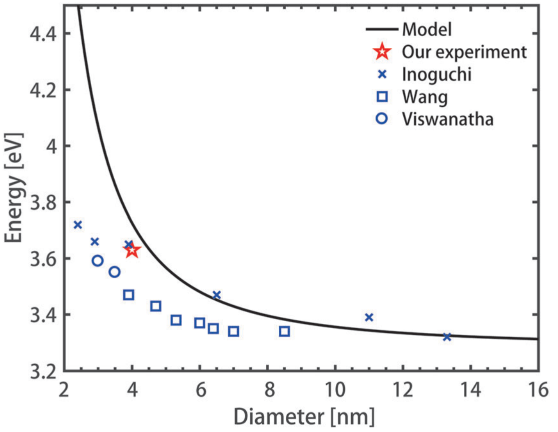

Fig. 3 Comparison of our work with previous ZnO nanocrystal reports, showing the dependence of bandgap energy on particle size. The model was proposed by Kayanuma *et al.* (ref. 45), and experimental results are from Inoguchi (ref. 26 and 49), Wang (ref. 32), and Viswanatha (ref. 27).

measured at 3.63 eV. We note that quantum confinement and the corresponding increase in the ZnO bandgap may be desirable in some applications and undesirable in others.

In this work, our goal is to produce ZnO nanocrystal inks that will enable the fabrication of high-performance printed electronics. This application has competing requirements: on one hand, the particles must be well-encapsulated to ensure the ink is stable over a period of weeks or months. On the other hand, the ligands must be easily removed after the ink is deposited onto a thin film to improve the electron transport through the film. In comparison to previous work on ZnO nanocrystals, we have demonstrated a synthesis procedure that results in improved surface control and solubility.[33,50] This suggests that the nanocrystal surfaces are well-encapsulated with ligands, which may also explain why our particles exhibit stronger quantum confinement than some previous work.[32] Viswanatha *et al.* employed a similar synthesis procedure,[27] but were not able to solubilize the particles using dodecanethiol ligands as we show here. Furthermore, we have observed that our ZnO nanocrystal ink has been shelf-stable with no changes observed in TEM for 7 months and counting (see ESI†). Ink stability is critically important for the large-scale adoption of printed electronics, and this demonstrates a key advantage of our nanocrystal inks over more commonly-employed sol–gels.

Characterization of solution-processed ZnO thin films using VASE

For the applications of ZnO we have discussed in the previous sections – from UV detectors to transistors to optical waveguides – a thin film of high-quality ZnO is required. Of course, the properties of the colloidal particles themselves are important, but only to the extent that they influence the fabrication of a thin-film device. TEM and UV-vis are essential tools for characterizing colloidal nanocrystal inks, but thin films made from these inks will often have significantly different properties than the solution itself. For instance, the absorption peak of our colloidal ZnO nanocrystals in solution was 3.63 eV, representing a 0.3 eV blue-shift from the bulk bandgap due to quantum confinement. When the nanocrystals are deposited onto a substrate, they will be in closer proximity to one another. Furthermore, thermal anneals and other common thin-film processing techniques will most likely remove the surface ligands that physically separate the nanocrystals, and it may cause the particles to fuse or melt. These factors may alter the degree of quantum confinement, and thus change the bandgap of the material. As previously mentioned, this has significant implications for the performance of electronic, optoelectronic, or photonic devices fabricated from the ZnO film. This is particularly true when the film has undergone some post-deposition treatment, such as the thermal sintering step that is common for the applications of interest here.

Thus, a simple yet robust method of characterizing the properties of solution-deposited thin films on any arbitrary substrate is critically important. Thin film UV-visible absorption measurements can provide some insight, but – as a transmission-mode method – samples and substrates often must be transparent. Instead, variable angle spectroscopic ellipsometry (VASE) is optimally suited for this task. VASE is a sensitive, non-destructive technique for determining the optical properties and microstructure of thin films. Woollam *et al.* provide a thorough review of this technique.[51] Briefly, VASE measures the change in a beam of reflected polarized light as a function of wavelength and incident angle. This technique can yield information for films only a few nanometers thick on nearly any arbitrary substrate. The directly-measured ellipsometric parameters are the relative amplitude change $\Psi(\lambda)$ and the relative phase change $\Delta(\lambda)$ of the light reflected from the sample. These two parameters are related to the material properties and are defined by[52]

$$\rho = r_\mathrm{p}/r_\mathrm{s} = \tan\Psi\,\mathrm{e}^{i\Delta} \tag{2}$$

where r_p and r_s are the complex Fresnel's reflection coefficients of the light polarized in the parallel and perpendicular planes, and ρ is the complex ratio of those coefficients. Because ellipsometry measures the ratio of these two values, it can be highly accurate and very reproducible. The measured ellipsometric parameters, Ψ and Δ, are used to produce a mathematical model that describes the interaction of light with the sample,[51] and optical constants can be extracted from the model. For our analysis, a two-step fitting process is used to determine optical constants for the ZnO thin film.[53,54] Ψ and Δ were measured over a wavelength range of 230 nm to 1200 nm using incident angles of 65°, 70°, and 75° with 2 nm step. The sample is modelled as a material stack composed of a silicon substrate, a thin silicon dioxide layer, and a layer with unknown optical constants representing the ZnO thin film under investigation. The ellipsometric data is then restricted to the spectral region in which the film is assumed to be transparent (approximately 600–1000 nm) and fit with a Cauchy–Urbach dispersion model. In the Cauchy–Urbach dispersion model, the refractive index $n(\lambda)$ and the extinction coefficient $k(\lambda)$ as a function of the wavelength are given by:[55–57]

$$n(\lambda) = A + \frac{B}{\lambda^2} + \frac{C}{\lambda^4} \tag{3}$$

$$k(\lambda) = \alpha^{\beta}\left[12\,400\left(\frac{1}{\lambda} - \frac{1}{\gamma}\right)\right] \tag{4}$$

These parameters in the dispersion model are the index parameters A, B, and C (which specify the index of refraction); the extinction coefficient amplitude α; the exponent factor β; and the band edge absorption parameter γ (which specifies the shape of the absorption tail). Each of these parameters can be defined as a variable fit parameter in the Cauchy layer, with an Urbach absorption. For our purposes C and γ are fixed at 0.00 and 340 nm,[58] respectively, while A, B, α, and β were selected as fit variables, along with the ZnO film thickness and native silicon dioxide thickness. Effective media approximations containing void spaces were found to not significantly affect the resulting fit parameters, and so were not included in the final model. The derived film thicknesses were then deselected as fit variables and the ellipsometric data was expanded to include the full spectral range of acquisition. A point-by-point fit of optical constants was then performed starting with the longest wavelength. The modelled ellipsometric parameters simulated from the optical constants derived in this manner are shown in Fig. 4, along with the experimentally measured data. The best-fit model is indistinguishable from the measured data (mean square error (MSE) of 0.86).

The optical constants obtained from VASE analysis are then used to determine the optical bandgap of our ZnO nanocrystal films. We first examined the properties of the ZnO film as-deposited onto the silicon wafer, without any additional post-deposition treatments. The absorption coefficient $\alpha(\lambda)$ was calculated from the relation

$$\alpha(\lambda) = \frac{4\pi k(\lambda)}{\lambda} \tag{5}$$

using $k(\lambda)$ obtained from the ellipsometric fitting procedure. As a direct bandgap material, the optical energy bandgap, E_g, of the ZnO nanocrystal thin film can be determined from the optical constants using Tauc's relation:[59]

$$(\alpha h\nu)^2 = B(h\nu - E_g) \tag{6}$$

where h is Planck's constant, ν is the frequency of the light, B is a proportionality constant, and E_g is the bandgap energy. For energies above the absorption edge, $(\alpha h\nu)^2$ is linear when plotted against $h\nu$, so extrapolation of the tangent line from high photon energy provides a measurement of the optical bandgap of the ZnO nanocrystals. Fig. 5 shows the determination of the optical bandgap of our ZnO nanocrystal film using Tauc's relation, where the absorption spectrum is predicted using VASE analysis. The optical bandgap obtained for 4 nm ZnO nanocrystals is 3.60 eV, which is in a very good agreement with the E_g value from UV-vis spectrum (3.63 eV). This is an important result: the significant blue shift of the bandgap confirms that the ZnO nanocrystals are still quantum confined after being deposited into a thin film.

Loss of quantum confinement after thermal anneal

Thermal processing steps are often required for printed electronics to improve the performance of conductors and semiconductors. The thermal process can remove impurities, densify the film, sinter nanoparticles, and even convert precursors into the desired material.[7,60–62] To determine the effect of these thermal anneals on the ZnO film properties, we used the same method outlined above to analyze two thin film samples that had undergone a thermal annealing treatment. The thin films were prepared using the same ZnO nanocrystals and with an identical deposition routine. The films were then annealed in a tube furnace for 90 minutes at 210 °C or 300 °C. Spectroscopic ellipsometry and the previously described method were used to extract the $k(\lambda)$ spectra for the annealed samples (see ESI†). Good model fits were obtained for the annealed ZnO films, with MSE value of 1.24 and 3.90 for the 210 °C and 300 °C samples, respectively.

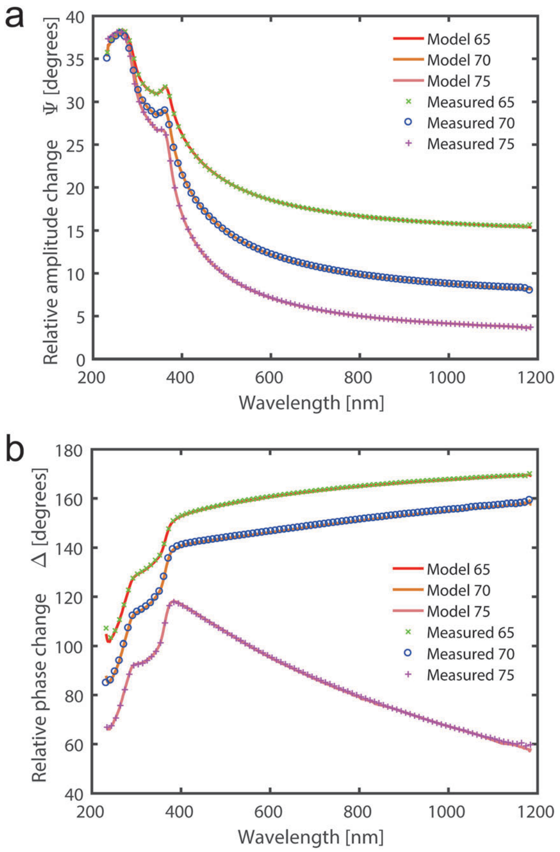

Fig. 4 Variable-angle spectroscopic ellipsometry (VASE) analysis of the as-prepared ZnO thin film. The relative amplitude change, Ψ, and the relative phase change, Δ, are shown in (a) and (b), respectively, for incident angles of 65°, 70°, and 75°. Experimental measurements (markers) and best-fit models (lines) confirm an excellent fit over the entire wavelength range.

The VASE analysis and the derived optical constants of the solution-processed ZnO thin films after a thermal anneal were used to extract the optical bandgap of the film. The results are shown in Fig. 5, and the annealed films are compared to the as-deposited film. It is notable that after a 300 °C tube furnace anneal, quantum confinement effects are no longer observed and the bulk bandgap of ZnO is recovered. This indicates that the quantum confinement barrier between ZnO nanocrystals has been removed.

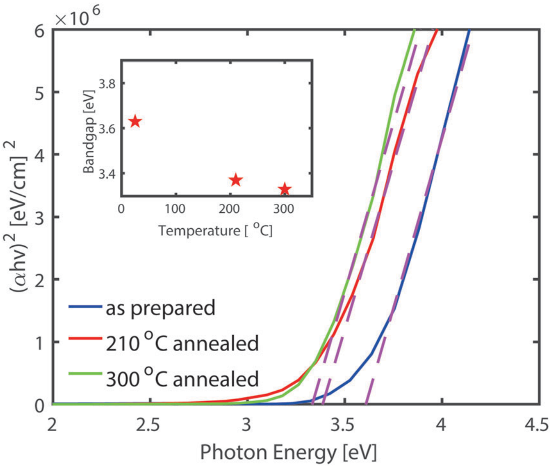

Fig. 5 Tauc plot showing $(\alpha h\nu)^2$ as a function of photon energy $h\nu$ for ZnO nanocrystal thin films as prepared, after 210 °C anneal, and after 300 °C anneal. The absorption coefficient, $\alpha(\lambda)$, for each film was calculated from the Cauchy–Urbach model obtained from VASE analysis. The inset summarizes the bandgap value of the ZnO film as a function of annealing temperature.

The first step in converting the as-deposited nanocrystals to a high-quality ZnO thin film is to remove the insulating ligands from the nanocrystal film, so we used FTIR to estimate the residual ligand content (1-dodecanethiol) in the film after the thermal annealing step. The 1-dodecanethiol is expected to exhibit strong C–H stretch vibration peaks around 2850 cm^{-1} and 2920 cm^{-1}. These peaks are prominently seen in the as-deposited ZnO film, indicating that the ligand molecules are still present in the film. This is consistent with the blue-shifted bandgap for the as-deposited film. The peaks attributed to the ligands are gradually reduced as the annealing temperature is increased (see Fig. 6), and by 210 °C the ligands are almost undetectable in the film. Again, this is consistent with the recovery of the bulk bandgap after the films are thermally annealed. The carbon content in the film was also measured with X-ray photoelectron spectroscopy (XPS). We confirmed that the carbon is significantly reduced following a 150 °C degree anneal, and it is below the detection limit after a 300 °C anneal (see ESI†). From these data, we conclude that the thermal annealing treatment is efficiently removing the surface ligands from the ZnO nanocrystals, thus removing the barriers between the particles. This is the first critical step towards achieving good electrical transport through the nanocrystal film, as required for printed electronics.

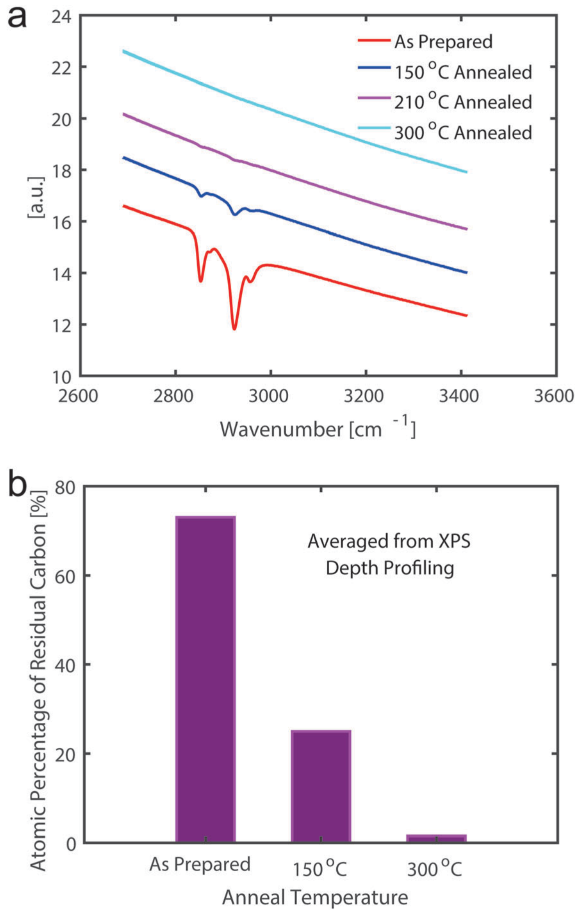

Fig. 6 (a) Infrared absorption (FTIR) spectra of ZnO nanocrystal thin films as a function of annealing temperature. (b) Average residual carbon percentage within the ZnO film from XPS depth profiling.

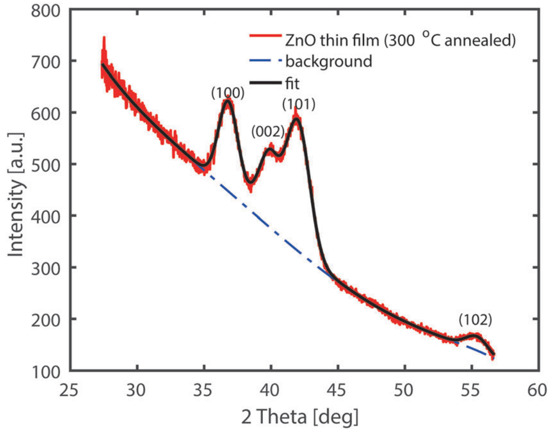

Fig. 7 Grazing incidence X-ray diffraction pattern of annealed ZnO nanocrystal thin film with Omega of 5 degrees (PDF no. 98-001-9461).

To characterize the crystal structure and crystallite size of our annealed ZnO thin films, we employed grazing incidence X-ray diffraction (GIXRD). GIXRD is a low-angle XRD technique that increases the path length of the radiation through a thin film compared to normal incidence XRD. This technique provides sufficient reflections to characterize very thin films of small nanocrystals, which are of great interest for printed electronics. Representative results of the GIXRD experiments and the fitted profile can be observed in Fig. 7. All the measurements are in good agreement with the expected XRD patterns of strain free zincite. Using the Scherrer formula and the broadening of all the GIXRD peaks, we have estimated a particle size of 5.5 ± 0.6 nm in the annealed ZnO films. The crystallite size is only slightly larger than the as-synthesized particles (4.0 ± 0.79 nm), which may indicate that 300 °C is a critical annealing temperature where the ZnO nanocrystals are just starting to grow. The lack of strain evident in the GIXRD data suggests that the randomly-oriented particles have not yet begun to fuse. As seen in Fig. 3, particles with a diameter of 5.5 nm are still predicted to exhibit quantum confinement ($E_g \sim 3.5$ eV). Interestingly, this quantum confinement is not observed in our ZnO films.

To examine the electron transport properties of the ZnO nanocrystal thin film, bottom-gate, top-contact thin film transistor (TFT) test structures were fabricated using photolithography, with the ZnO nanocrystal solution as the channel material. The ZnO films were annealed at 300 °C for 1 hour with a final thickness of 30 nm. Heavily-doped silicon wafers with 50 nm thermally grown SiO_2 were used as the gate electrode and gate oxide, respectively, and 100 nm Al was deposited as source/drain electrodes.

The transfer and output characteristics of the TFT are shown in Fig. 8. The devices operate in depletion mode with a small negative turn-on voltage. Clear saturation of the output curves is observed, with some noticeable hysteresis. The average field effect mobility in the linear region (as extracted following the standard square law model) is ~ 0.002 cm^2 V^{-1} s^{-1} and the I_{ON}/I_{OFF} ratio is $\sim 10^4$. This device performance is consistent with previous reports of solution-processed ZnO TFTs annealed at low to moderate temperatures.[63,64] Importantly, the onset of TFT behaviour shown here is consistent with our hypothesis that removing the nanocrystal ligands by annealing the films at 300 °C has removed the most significant barrier to transport. Device performance could be further optimized by using a higher annealing temperature and/or a high-κ gate dielectric.

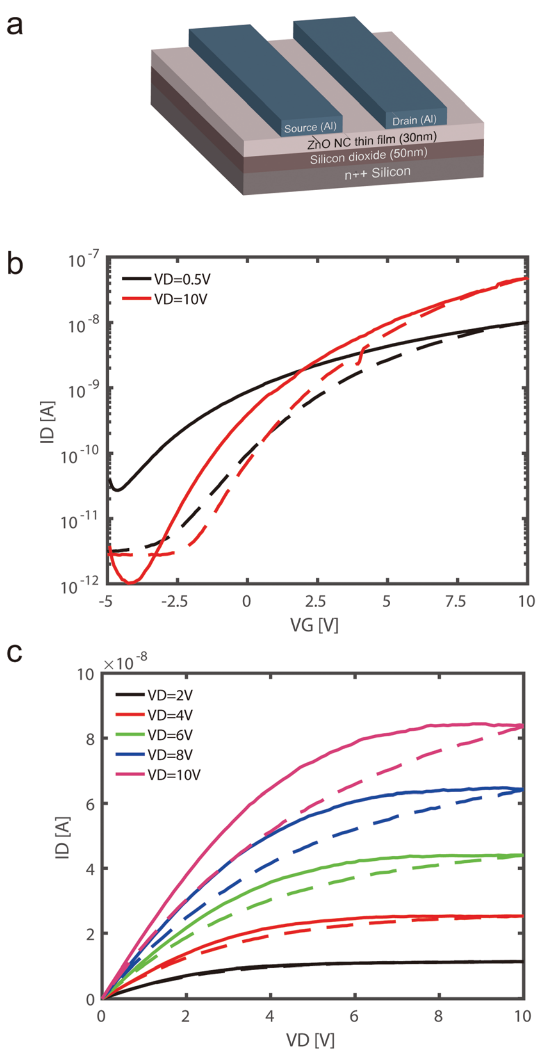

Fig. 8 (a) Structure of the back-gate, top-contact ZnO nanocrystal TFT. (b) Transfer characteristics and (c) output characteristics of a TFT utilizing the ZnO nanocrystals as the channel layer, after a 300 °C annealing.

Conclusions

We report a nanocrystal synthesis and purification routine that yields monodisperse, well-encapsulated wurtzite ZnO nanocrystals with an average diameter of 4.0 ± 0.79 nm. The absorption peak of the colloidal solution is at 3.63 eV, a ~0.3 eV blue shift from the bulk bandgap of ZnO. This increase in the bandgap is in good agreement with the quantum confinement effects that are expected based on well-accepted models of nanocrystal size *vs.* bandgap energy. Our results are a closer match to the model than several other studies of ultra-small particles. We hypothesize that the extra degree of quantum confinement results from the fact that our particles are highly crystalline and well-encapsulated. This hypothesis is supported by TEM and by the excellent solubility and stability of our ZnO inks. The degree of quantum confinement may be useful as one measure of the quality of a nanocrystal ink because small, uniform, well-encapsulated particles are desirable for printed electronics.

However, while strong quantum confinement may be correlated to desirable ink properties, it is generally not desirable for ZnO thin-film electronics. We have shown that VASE analysis is a powerful tool that can be used to characterize the degree of quantum confinement in nanocrystal thin films on arbitrary substrates. We use a combination of VASE, FTIR, XPS, and GIXRD to monitor quantum confinement, residual ligand content, and crystallinity during the deposition and annealing processes. We show that these tools provide important insight to the fabrication of printed ZnO thin-films. First, we observe that the absorption peak of the colloidal solution (3.63 eV) closely matches the bandgap extracted from VASE analysis of the as-deposited film (3.60 eV); this indicates that the quantum confinement of the ZnO nanocrystals is maintained when the particles are deposited onto the substrate. Second, we observe that thermal annealing treatments gradually reduce the ZnO bandgap to the bulk value (3.3 eV) while removing the nanocrystal ligands, resulting in a phase-pure and strain-free ZnO nanocrystalline film with low carbon contamination. The loss of quantum confinement is a positive result with regards to printed ZnO films for TFT applications. A larger bandgap would result in a lower free electron concentration in the ZnO, which would degrade TFT performance. Third, we find that the loss of quantum confinement does not require significant crystallite growth, which means that efficient electron transport through the film can be achieved by simply removing the ligands. ZnO nanocrystal TFTs annealed at 300 °C – the temperature at which ligands are removed – exhibited a field effect mobility of $\sim 0.002\ \text{cm}^2\ \text{V}^{-1}\ \text{s}^{-1}$. This opens many doors for non-thermal processing routes for high-quality printed electronics on low-cost plastic substrates.

More broadly, these promising results demonstrate that semiconductor thin films can be controlled by leveraging the benefits of colloidal nanocrystal inks for printed electronics. These techniques will continue to provide insight into the intelligent design of semiconductor nanocrystal inks for solution-processed thin films, especially as new surface chemistries and post-deposition treatments are explored to simultaneously improve the semiconductor quality and reduce the thermal processing budget for printed electronics.

Conflicts of interest

There are no conflicts to declare.

Acknowledgements

This work was supported partially by the National Science Foundation through the University of Minnesota MRSEC under Award Number DMR-1420013, and also under Award Number ECCS-1710008. Part of this work was carried out in the College of Science and Engineering Characterization Facility, University of Minnesota, which has received capital equipment funding from the NSF through the UMN MRSEC program under Award Number DMR-1420013. This work was also supported in part by the Office of the Vice President for Research and the MnDRIVE RSAM Initiative, University of Minnesota.

References

1 X. L. Dai, Z. X. Zhang, Y. Z. Jin, Y. Niu, H. J. Cao, X. Y. Liang, L. W. Chen, J. P. Wang and X. G. Peng, *Nature*, 2014, **515**, 96–99.

2 G. Konstantatos, J. Clifford, L. Levina and E. H. Sargent, *Nat. Photonics*, 2007, **1**, 531–534.

3 B. Sun and H. Sirringhaus, *Nano Lett.*, 2005, **5**, 2408–2413.

4 D. B. Mitzi, *J. Mater. Chem.*, 2004, **14**, 2355–2365.

5 C. L. Tan, Z. D. Liu, W. Huang and H. Zhang, *Chem. Soc. Rev.*, 2015, **44**, 2615–2628.

6 S. R. Thomas, P. Pattanasattayavong and T. D. Anthopoulos, *Chem. Soc. Rev.*, 2013, **42**, 6910–6923.

7 S. L. Swisher, S. K. Volkman and V. Subramanian, *ACS Appl. Mater. Interfaces*, 2015, **7**, 10069–10075.

8 D. V. Talapin, J. S. Lee, M. V. Kovalenko and E. V. Shevchenko, *Chem. Rev.*, 2010, **110**, 389–458.

9 M. V. Kovalenko, L. Manna, A. Cabot, Z. Hens, D. V. Talapin, C. R. Kagan, V. I. Klimov, A. L. Rogach, P. Reiss, D. J. Milliron, P. Guyot-Sionnnest, G. Konstantatos, W. J. Parak, T. Hyeon, B. A. Korgel, C. B. Murray and W. Heiss, *ACS Nano*, 2015, **9**, 1012–1057.

10 N. S. Pesika, Z. S. Hu, K. J. Stebe and P. C. Searson, *J. Phys. Chem. B*, 2002, **106**, 6985–6990.

11 J. Zhou, Y. D. Gu, Y. F. Hu, W. J. Mai, P. H. Yeh, G. Bao, A. K. Sood, D. L. Polla and Z. L. Wang, *Appl. Phys. Lett.*, 2009, 94.

12 Y. Z. Jin, J. P. Wang, B. Q. Sun, J. C. Blakesley and N. C. Greenham, *Nano Lett.*, 2008, **8**, 1649–1653.

13 A. Bera and D. Basak, *ACS Appl. Mater. Interfaces*, 2009, **1**, 2066–2070.

14 J. Gilot, I. Barbu, M. M. Wienk and R. A. J. Janssen, *Appl. Phys. Lett.*, 2007, 91.

15 W. J. E. Beek, M. M. Wienk and R. A. J. Janssen, *Adv. Mater.*, 2004, **16**, 1009–1013.

16 X. J. Huang and Y. K. Choi, *Sens. Actuators, B*, 2007, **122**, 659–671.

17 J. P. Wang, B. Q. Sun, F. Gao and N. C. Greenham, *Phys. Status Solidi A*, 2010, **207**, 484–487.

18 K. Mohanta and A. J. Pal, *J. Appl. Phys.*, 2009, **105**, 7.

19 S. Chu, G. P. Wang, W. H. Zhou, Y. Q. Lin, L. Chernyak, J. Z. Zhao, J. Y. Kong, L. Li, J. J. Ren and J. L. Liu, *Nat. Nanotechnol.*, 2011, **6**, 506–510.

20 Y. S. Rim, H. J. Chen, X. L. Kou, H. S. Duan, H. P. Zhou, M. Cai, H. J. Kim and Y. Yang, *Adv. Mater.*, 2014, **26**, 4273–4278.

21 J. Socratous, K. K. Banger, Y. Vaynzof, A. Sadhanala, A. D. Brown, A. Sepe, U. Steiner and H. Sirringhaus, *Adv. Funct. Mater.*, 2015, **25**, 1873–1885.

22 R. A. Street, T. N. Ng and R. A. Lujan, *ACS Appl. Mater. Interfaces*, 2014, **6**, 4428–4437.

23 K. H. Liu, T. C. Chang, K. C. Chang, T. M. Tsai, T. Y. Hsieh, M. C. Chen, B. L. Yeh and W. C. Chou, *Appl. Phys. Lett.*, 2014, **104**, 4.

24 U. Ozgur, Y. I. Alivov, C. Liu, A. Teke, M. A. Reshchikov, S. Dogan, V. Avrutin, S. J. Cho and H. Morkoc, *J. Appl. Phys.*, 2005, **98**, 103.

25 V. Subramanian, J. L. Cen, A. D. Vornbrock, G. Grau, H. Kang, R. Kitsomboonloha, D. Soltman and H. Y. Tseng, *Proc. IEEE*, 2015, **103**, 567–582.

26 M. Inoguchi, K. Suzuki, K. Kageyama, H. Takagi and Y. Sakabe, *J. Am. Ceram. Soc.*, 2008, **91**, 3850–3855.

27 R. Viswanatha, S. Sapra, B. Satpati, P. V. Satyam, B. N. Dev and D. D. Sarma, *J. Mater. Chem.*, 2004, **14**, 661–668.

28 M. A. Mahjoub, G. Monier, C. Robert-Goumet, F. Reveret, M. Echabaane, D. Chaudanson, M. Petit, L. Bideux and B. Gruzza, *J. Phys. Chem. C*, 2016, **120**, 11652–11662.

29 Y. V. Panasiuk, O. E. Raevskaya, O. L. Stroyuk, S. Y. Kuchmiy, V. M. Dzhagan, M. Hietschold and D. R. T. Zahn, *Nanotechnology*, 2014, **25**, 11.

30 A. Wood, M. Giersig, M. Hilgendorff, A. Vilas-Campos, L. M. Liz-Marzan and P. Mulvaney, *Aust. J. Chem.*, 2003, **56**, 1051–1057.

31 S. Mahamuni, K. Borgohain, B. S. Bendre, V. J. Leppert and S. H. Risbud, *J. Appl. Phys.*, 1999, **85**, 2861–2865.

32 Y. S. Wang, P. J. Thomas and P. O'Brien, *J. Phys. Chem. B*, 2006, **110**, 4099–4104.

33 K. Suzuki, H. Kondo, M. Inoguchi, N. Tanaka, K. Kageyama and H. Takagi, *Appl. Phys. Lett.*, 2009, **94**, 3.

34 J. Hambrock, S. Rabe, K. Merz, A. Birkner, A. Wohlfart, R. A. Fischer and M. Driess, *J. Mater. Chem.*, 2003, **13**, 1731–1736.

35 H. Kang, R. Kitsomboonloha, J. Jang and V. Subramanian, *Adv. Mater.*, 2012, **24**, 3065–3069.

36 P. Buffat and J. P. Borel, *Phys. Rev. A: At., Mol., Opt. Phys.*, 1976, **13**, 2287–2298.

37 S. K. Volkman, B. A. Mattis, S. E. Molesa, J. B. Lee, A. de la F. Vornbrock, T. Bakhishev and V. Subramanian, *Electron Devices Meeting, IEDM Technical Digest, IEEE International*, 2004, pp. 769–772.

38 L. Polavarapu, K. K. Manga, K. Yu, P. K. Ang, H. D. Cao, J. Balapanuru, K. P. Loh and Q. H. Xu, *Nanoscale*, 2011, **3**, 2268–2274.

39 P. Peng, A. Hu and Y. Zhou, *Appl. Phys. A: Mater. Sci. Process.*, 2012, **108**, 685–691.

40 A. Kocjan, M. Logar and Z. J. Shen, *Sci. Rep.*, 2017, 7.

41 U. Koch, A. Fojtik, H. Weller and A. Henglein, *Chem. Phys. Lett.*, 1985, **122**, 507–510.

42 E. A. Meulenkamp, *J. Phys. Chem. B*, 1998, **102**, 5566–5572.

43 M. H. Huang, S. Mao, H. Feick, H. Q. Yan, Y. Y. Wu, H. Kind, E. Weber, R. Russo and P. D. Yang, *Science*, 2001, **292**, 1897–1899.

44 A. B. Djurisic and Y. H. Leung, *Small*, 2006, **2**, 944–961.

45 Y. Kayanuma, *Phys. Rev. B: Condens. Matter Mater. Phys.*, 1988, **38**, 9797–9805.

46 M. K. Wu, Y. T. Shih, M. J. Chen, J. R. Yang and M. Shiojiri, *Phys. Status Solidi RRL*, 2009, **3**, 88–90.

47 B. X. Lin, Z. X. Fu and Y. B. Jia, *Appl. Phys. Lett.*, 2001, **79**, 943–945.

48 Y. W. Heo, D. P. Norton, L. C. Tien, Y. Kwon, B. S. Kang, F. Ren, S. J. Pearton and J. R. LaRoche, *Mater. Sci. Eng., R*, 2004, **47**, 1–47.

49 M. Inoguchi, K. Suzuki, N. Tanaka, K. Kageyama and H. Takagi, *J. Mater. Res.*, 2009, **24**, 2243–2251.

50 D. Kim, Y. Jeong, K. Song, S. K. Park, G. Z. Cao and J. Moon, *Langmuir*, 2009, **25**, 11149–11154.

51 J. A. Woollam, J. N. Hilfiker, T. E. Tiwald, C. L. Bungay, R. A. Synowicki, D. E. Meyer, C. M. Herzinger, G. L. Pfeiffer, G. T. Cooney and S. E. Green, *Optical Metrology Roadmap for the Semiconductor, Optical, and Data Storage Industries, SPIE-Int. Soc. Optical Engineering*, 2000, vol. 4099, pp. 197–205.

52 A. Hashimoto, A. G. Bhuiyan and A. Yamamoto, *J. Appl. Phys.*, 2003, **94**, 2779.

53 M. Gilliot, C. Eypert and A. Hadjadj, *J. Appl. Phys.*, 2013, **114**, 6.

54 *Guide to Using WVASE 32: Spectroscopic Ellipsometry Data Acquisition and Analysis Software*, J. A. Woollam Company, Incorporated, 2008.

55 D. J. Schroeder, *J. Opt. Soc. Am.*, 1962, **52**, 1380–1386.

56 J. I. Pankove, *Semicond. Semimetals*, 1984, **21**, 1–10.

57 S. Adachi, *Optical Properties of Crystalline and Amorphous Semiconductors, Materials and Fundamental Principles*, Springer, US, 1999.

58 J. M. Khoshman and M. E. Kordesch, *Thin Solid Films*, 2007, **515**, 7393–7399.

59 J. G. Tauc, R. Grigorovici and A. Vancu, *Phys. Status Solidi B*, 1966, **15**, 627.

60 X. G. Wang, W. M. Guo and G. J. Zhang, *Scr. Mater.*, 2009, **61**, 177–180.

61 R. Y. Yang, M. H. Lin and H. Y. Lu, *Acta Mater.*, 2001, **49**, 2597–2607.

62 C. K. Xu, J. M. Wu, U. V. Desai and D. Gao, *Nano Lett.*, 2012, **12**, 2420–2424.

63 J. H. Jun, B. Park, K. Cho and S. Kim, *Nanotechnology*, 2009, **20**, 6.

64 H. Bong, W. H. Lee, D. Y. Lee, B. J. Kim, J. H. Cho and K. Cho, *Appl. Phys. Lett.*, 2010, **96**, 3.